An approach for predicting stress-induced anisotropy around a borehole

Xinding Fang[1], Michael Fehler[1], Zhenya Zhu[1], Tianrun Chen[2], Stephen Brown[1], Arthur Cheng[2] and M. Nafi Toksöz[1]

[1]*Dept. of Earth, Atmospheric and Planetary Sciences*

Massachusetts Institute of Technology

77 Masschusetts Avenue Cambridge, MA 02139

[2]*Halliburton*

3000 N Sam Houston Pkwy E, Houston TX 77032

(May 3, 2012)

Running head: **Borehole stress-induced anisotropy**

ABSTRACT

Formation elastic properties near a borehole may be altered from their original state due to the stress concentration around the borehole. This could result in a biased estimation of formation properties but could provide a means to estimate *in situ* stress from sonic logging data. In order to properly account for the formation property alteration, we propose an iterative numerical approach to calculate the stress-induced anisotropy around a borehole by combining the rock physics model of Mavko et al. (1995) and a finite-element method. We show the validity and accuracy of our approach by comparing numerical results to laboratory measurements of the stress-strain relation of a sample of Berea sandstone, which contains a borehole and is subjected to uniaxial stress loading. Our iterative approach converges very fast and can be applied to calculate the spatially varying stiffness tensor of

the formation around a borehole for any given stress state.

INTRODUCTION

Borehole logging data provide an important way to interpret the rock anisotropy and estimate the *in situ* stress state (Mao, 1987; Sinha and Kostek, 1995). Typically, the anisotropy in intact rocks includes intrinsic and stress-induced components (Jaeger et al., 2007). Intrinsic anisotropy can be caused by bedding, microstructure, or aligned fractures, while stress-induced anisotropy is caused by the opening or closing of the compliant and crack-like parts of the pore space due to tectonic stresses. Most unfractured reservoir rocks, such as sands, sandstones and carbonates, have very little intrinsic anisotropy in an unstressed state (Wang, 2002). Drilling a borehole in a formation significantly alters the local stress distribution. This causes the closure or opening of cracks in rocks around the borehole and leads to an additional stress-induced anisotropy. In order to properly include this additional stress-induced anisotropy during inversion for formation properties and the *in situ* stress estimation from logging data, a thorough analysis needs to consider the constitutive relation between the complex stress field applied around a borehole and the stiffness tensor of a rock with micro-cracks embedded in the matrix (Brown and Cheng, 2007).

Three theoretical approaches have been proposed to calculate the stress-related anisotropy around a borehole. The first approach (Sinha and Kostek, 1996; Winkler et al., 1998) used the acoustoelastic model to calculate the stress-induced azimuthal anisotropy around a borehole. The velocity variation with applied stresses is accounted for through the use of the third order elastic constants, which are obtained through compression experiments on rock samples. The second approach (Tang et al., 1999; Tang and Cheng, 2004) used an empirical stress-velocity coupling relation to estimate the variation of shear elastic constants (C_{44} and C_{55}) as a function of stress. In this approach, the square of the shear wave velocities propa-

gating along a borehole with different polarizations are assumed to be linearly proportional to the stresses applied normal to the borehole axis. This approach is used for studying shear wave splitting in a borehole and only gives the values of shear elastic constants (*i.e,* C_{44} and C_{55}) instead of the full elastic stiffness tensor. The first two approaches are based on an assumption of plane strain, which considers formation properties to be invariant along the borehole axis and that applied stresses are normal to the borehole axis. Brown and Cheng (2007) proposed the third approach to calculate stress-induced anisotropy around a borehole embedded in an *anisotropic* medium. In their model, the stress-dependent stiffness tensor of anisotropic rocks is calculated using a general fabric tensor model (Oda et al., 1986; Oda, 1986). The general fabric tensor model requires the prior knowledge of crack geometries (*i.e,* crack shapes and aspect ratio spectra) and distributions, which may not always be available in the field applications. In this paper, we replace the general fabric tensor model with the model of Mavko et al. (1995), which assumes the crack orientation distribution in the rock matrix in an unstressed state to be uniform and isotropic. Under this assumption, rocks are still isotropic when subjected to a hydrostatic stress and become anisotropic under an uniaxial or a biaxial stress loading. Anisotropy is induced through closing the preferentially-aligned cracks. The detailed information about cracks is not required in Mavko's model and the effect of crack *closure* is implicitly determined by the relation between elastic wave velocities of the rock and the applied hydrostatic compression pressure using laboratory data. Another major assumption of Mavko's model is that the anisotropy induced by crack *opening* is negligible.

BRIEF REVIEW OF MAVKO'S METHOD

Mavko et al. (1995) proposed a simple and practical method to estimate the generalized

pore space compliance of rocks using experimental data of rock velocity versus hydrostatic pressure. The approach proposed by Mavko et al. (1995) for calculating the stiffness tensor with stress-induced anisotropy at a stress state σ is described below:

(1) Calculate the pressure-dependent isotropic elastic compliances $S^{iso}_{ijkl}(p)$ from measurements of compressional (P) and shear wave (S) velocities versus hydrostatic pressure. The compliance S^{0}_{ijkl} at the largest measured pressure, under which most of the compliant parts of the pore space are closed, is chosen as a reference point. The additional compliance $\Delta S^{iso}_{ijkl}(p)$ due to the presence of pore space at pressure p is defined to be $S^{iso}_{ijkl}(p) - S^{0}_{ijkl}$. Note that at a pressure p less than the largest measured pressure, there is more pore volume than at the highest pressure and the compliance is larger.

(2) Calculate the pressure-dependent crack normal compliance $W_N(p)$ and crack tangential compliance $W_T(p)$ from $\Delta S^{iso}_{ijkl}(p)$ via

$$W_N(p) = \frac{1}{2\pi}\Delta S^{iso}_{jjkk}(p) \tag{1}$$

and

$$W_T(p) = W_N(p) \cdot \frac{\Delta S^{iso}_{jkjk}(p) - \Delta S^{iso}_{jjkk}(p)}{4\Delta S^{iso}_{jjkk}(p)}, \tag{2}$$

where the repeated indices in ΔS^{iso}_{jjkk} and ΔS^{iso}_{jkjk} mean summation, the factor $\frac{1}{2\pi}$ comes from the average of crack compliance over all solid angles.

(3) Calculate the stress-induced compliance $\Delta S_{ijkl}(\sigma)$ through

$$\begin{aligned}\Delta S_{ijkl}(\sigma) \;=\; & \int_{\theta=0}^{\pi/2}\int_{\phi=0}^{2\pi} W_N(\mathbf{m}^T\sigma\mathbf{m}) m_i m_j m_k m_l \sin\theta d\theta\phi \\ & + \int_{\theta=0}^{\pi/2}\int_{\phi=0}^{2\pi} W_T(\mathbf{m}^T\sigma\mathbf{m})[\delta_{ik}m_j m_l + \delta_{il}m_j m_k \\ & + \delta_{jk}m_i m_l + \delta_{jl}m_i m_k - 4m_i m_j m_k m_l]\sin\theta d\theta d\phi \end{aligned} \tag{3}$$

where σ is a 3×3 stress tensor, $\mathbf{m} \equiv (\sin\theta\cos\phi, \sin\theta\sin\phi, \cos\theta)^T$ is the unit normal to the crack surface, θ and ϕ are the polar and azimuthal angles in a spherical coordinate system.

Note that $W_N(p)$ and $W_N(p)$ in equations 1 and 2 have been replaced by $W_N(\mathbf{m}^T\sigma\mathbf{m})$ and $W_T(\mathbf{m}^T\sigma\mathbf{m})$ in equation 3, assuming that the crack closure is mainly determined by the normal stress, $\mathbf{m}^T\sigma\mathbf{m}$, acting on crack surface. The stress tensor σ needs to be projected onto the normal directions of the crack surfaces.

(4) Obtain the stiffness tensor $C_{ijkl}(\sigma)$ by inverting $S^0_{ijkl} + \Delta S_{ijkl}(\sigma)$.

WORKFLOW OF THE NUMERICAL MODELING

The method of Mavko et al. (1995) can be applied to calculate the stress-induced anisotropy in homogeneous rocks, as discussed in the introduction. When a borehole is drilled in a rock subjected to an uniaxial stress, the local stress field around the borehole is changed and causes anisotropy. Similar to the procedure proposed by Brown and Cheng (2007), in this paper, we investigate this stress-induced anisotropy around a borehole at a given stress state by combining the method of Mavko et al. (1995) and a numerical approach illustrated in Figure 1.

We first begin with a homogeneous isotropic intact rock model, on which Mavko's model is based. The intact rock refers to the rock before drilling a borehole. After experimentally obtaining the P and S-wave velocity data as a function of hydrostatic pressure, we apply equation 3 to calculate the anisotropic stiffness tensor $C_{ijkl}(\sigma)$ of the intact rock under stress σ, which can be anisotropic. Next, we drill a borehole in the model and use the calculated $C_{ijkl}(\sigma)$ as the input in our initial model containing a borehole. The current $C_{ijkl}(\sigma)$ does not include the effect from stress change due to the borehole. We apply a finite-element method (FEM) to calculate the spatially varying stress field within the model including the borehole for a given stress loading σ and the initial anisotropic $C_{ijkl}(\sigma)$. From the output of FEM, we can obtain the local stress tensor $\sigma(\mathbf{x})$ and then calculate a new elastic

tensor $C_{ijkl}(\sigma, \mathbf{x})$ as a function of space applying equation 3. The new $C_{ijkl}(\sigma, \mathbf{x})$ becomes anisotropic and includes the effect of the borehole. We keep iterating the above steps by calling FEM and applying equation 3 until $C_{ijkl}(\sigma, \mathbf{x})$ converges. We use the following as a convergence criterion

$$\text{Convergence}(m) = \frac{1}{N}\sum_{n=1}^{N}\sqrt{\frac{\sum_{ijkl}\left[C^{m}_{ijkl}(\mathbf{x}_n) - C^{m-1}_{ijkl}(\mathbf{x}_n)\right]^2}{\sum_{ijkl}\left[C^{m-1}_{ijkl}(\mathbf{x}_n)\right]^2}} \tag{4}$$

where m indicates the m^{th} iteration, N is the total number of spatial sampling points of the model, $\sum_{ijkl}$ means the summation over 21 independent elastic constants, Convergence(m) indicates the percentage change of the model stiffness after the m^{th} iteration comparing to the model at the $(m-1)^{\text{th}}$ iteration. We define C_{ijkl} to have converged when Convergence$(m) < 1\%$. Convergence means that C_{ijkl} and the stress are consistent and Hooke's law is satisfied, the model is under static equilibrium. Finally, we can obtain the spatial distribution of the anisotropic elastic constants $C_{ijkl}(\sigma, \mathbf{x})$ around a borehole for the given stress state as the output of our numerical model.

In our approach, we assume that stress induced anisotropy is caused by the closure of cracks due to the applied compressive stress on cracks' surfaces and the effect of tensile stress is negligible. This assumption brings out two issues: (1) how important is the tensile stress in the earth? (2) how do we deal with the tensile stress in our calculation? We will discuss these below.

For a homogeneous isotropic elastic rock, the circumferential stress σ_θ and the radial stress σ_r around a circular borehole subjected to minimum and maximum principal stresses (S_h and S_H) are given by (for example, Tang and Cheng (2004))

$$\sigma_\theta = \frac{1}{2}(S_H + S_h)\left(1 + \frac{R^2}{r^2}\right) - \frac{1}{2}(S_H - S_h)\left(1 + 3\frac{R^4}{r^4}\right)\cos 2\theta \tag{5}$$

$$\sigma_r = \frac{1}{2}(S_H + S_h)\left(1 - \frac{R^2}{r^2}\right) + \frac{1}{2}(S_H - S_h)\left(1 - 4\frac{R^2}{r^2} + 3\frac{R^4}{r^4}\right)\cos 2\theta \qquad (6)$$

where R is borehole radius, r is the distance from the center of the borehole, θ is azimuth measured from the direction of S_H.

The compressive stress $\sigma_\theta + \sigma_r$ around the borehole provides an indication of how velocity around the borehole is affected by stress concentration. $\sigma_\theta + \sigma_r$ has maximum and minimum values at the wellbore, and σ_r=0 at r=R, so the stress field at the wellbore is dominated by σ_θ, which has the maximum value $\sigma_\theta = 3S_H - S_h$ at $\theta = \pm 90^0$ and the minimum value $\sigma_\theta = 3S_h - S_H$ at $\theta = 0^0$ and 180^0. *In situ*, both S_H and S_h are present, and $S_H \leq 3S_h$ in most case (Zoback et al., 1985; Brace and Kohlstedt, 1980), thus the minimum $\sigma_\theta = 3S_h - S_H \geq 0$ is compressive. In this sense, there is no tensile stress around the borehole.

However, the condition $S_H \leq 3S_h$ may not be satisfied in the laboratory experiments. Uniaxial compression experiments (*i.e.* S_h=0), which would induce significant tensile stress around the borehole, have been conducted for the study of stress induced velocity change around a borehole by many researchers (Winkler, 1996; Winkler et al., 1998; Tang and Cheng, 2004). The change of rock elastic properties caused by tensile stress is usually unknown. Traditional methods (Sinha and Kostek, 1996; Tang et al., 1999) for calculating the stress dependent velocity around a borehole use the data measured from compression experiments to estimate either the third order elastic constants or empirical coefficients, which relate the rock velocity change to the applied stresses. For the case of uniaxial stress, they based their equations on compression experiment data to predict the velocity in the tensile stress regions, this kind of extrapolation has no physical basis and could result in underestimation of the velocity in the regions around $\theta = 0^0$ and 180^0. A schematic expla-

nation is shown in Figure 2a. The solid curve represents the data measured in compressive experiment, and dash curve indicates the extrapolation of the data to the tensile stress (stress<0) region, which may incorrectly predict low velocity in this region. Different kinds of rock would respond to tensile stress differently due to varying microcrack structure and rock strength. For Berea sandstone, which is used in our experiments, tensile stresses are relatively less efficient in opening microcracks (Winkler, 1996). We assume the rock elastic constants under tensile stress remain the same as in a zero stress state in our calculation, shown as the dashed line in Figure 2b, in other words, crack opening is neglected. Our results will show that good results can be obtained with this assumption on Berea sandstone.

LABORATORY EXPERIMENT

In this section, we present results from static strain measurement on a Berea sandstone under uniaxial loading to verify the validity and reliability of our numerical approach. The dimensions of the Berea sandstone sample used in this experiment are $10\times10\times10$ cm. P and S-wave velocities of the unstressed rock sample were measured in three directions. Figure 3 shows the measured P-waves and S-waves in three orthogonal directions. We pick the first breaks from the trace data and calculate the P and S-wave velocities and find that P-wave and S-wave anisotropy are only 0.7% and 1.8%, respectively. The measured parameters of the rock are summarized in Table 1.

First, we measure P and S-wave velocities under varying hydrostatic stress. These data are used to estimate the normal and tangential crack compliances as functions of hydrostatic pressure, which are required by the method of Mavko et al. (1995). Then, we perform strain-stress measurements of the intact rock under uniaxial loading. This step is to benchmark our measurement setup with the Mavko et al. (1995) model. Finally, we

measure the strain-stress behavior of the rock containing a borehole subjected to a gradually increasing uniaxial stress and compare it with our numerical calculations.

Measurement of P and S-wave velocities under hydrostatic compression

In order to measure P and S-wave velocities versus hydrostatic pressure, we cut a 2 inch long and 1 inch diameter cylindrical core from our rock sample that will also be used for the subsequent experiments. We measured P and S-wave velocities parallel to the core axis. The S-wave velocity measurements were made using two orthogonal polarization directions, as shown in Figure 4. The velocity and hydrostatic pressure have the following empirical relation (Birch, 1960)

$$V = a \cdot \log P + b, \tag{7}$$

where V represents both compressional and shear velocities and P is hydrostatic pressure, a and b are coefficients related to the porosity and mineralogy of the rock. We find that equation 7 can not fit the hydrostatic data very well for pressure < 1 MPa, so we modify equation 7 to equation 8 as

$$V = \begin{cases} a_1 \cdot P + b_1, & P \leq 1 \text{ MPa} \\ a_2 \cdot \log P + b_2, & P > 1 \text{ MPa} \end{cases} \tag{8}$$

where a_1, b_1, a_2 and b_2 are constants to be determined through least-squares method by adding the constraint that the two fitting functions are equal at P=1 MPa. The fits to the P and S-wave velocities (average of S_1 and S_2) are shown as the blue and red curves, respectively, in Figure 4. Given equation 8, we can now analytically calculate the P and S-velocities at any given hydrostatic pressure.

Strain measurement of intact rock under uniaxial stress

In the intact rock experiment, four two-component strain gages were mounted at different positions on the rock sample for measuring the normal strains in the directions parallel and normal to the direction of loading stress, as shown in Figure 5 (a photo of our experiment setup). We use standard amplified wheatstone bridge circuits with an analog-to-digital converter to collect signals from all strain gages simultaneously. Before performing the experiment, the rock was stress-cycled several times in order to minimize hysteresis. During the experiment, the uniaxial loading stress was gradually raised from 0 to 10.6 MPa in steps of 0.96 MPa. We limited the maximum loading stress to 10.6 MPa to prevent permanent deformation in the rock. The strains measured under uniaxial loading at four strain gages were almost the same. This suggests that the loading stress was evenly distributed on the rock surface.

Figure 6 shows the comparison between the strains (black solid curves) calculated using the method of Mavko et al. (1995) and the measured strains (solid and empty squares). In the direction parallel to the loading axis, the black solid curve (calculated values) matches the solid squares (measured data) very well. In the direction normal to the loading axis, the measured data (empty squares) seem larger than the calculated values, especially at higher loading stress ranges. This could be caused by neglecting the effects of the opening of new cracks aligned parallel with the loading axis (Sayers et al., 1990; Mavko et al., 1995). The dashed curves, which are shown for comparison, are the strain values calculated under the assumption that rock properties remain isotropic during the experiment but V_P and V_S are given by equation 8 in different stress state, which is corresponding to hydrostatic compression and will be referred to as the isotropic model hereafter. The absolute values

of these dashed curves are always smaller than those of the solid curves. For the isotropic model, the normal stress causes the closure of all cracks independent of orientation, while the anisotropic model assumes smaller closure of cracks oriented in directions not perpendicular to the loading direction. Therefore, hydrostatic compression leads to a stiffer rock compared to the rock under uniaxial stress.

Strain measurement of the rock with a borehole under uniaxial loading

A borehole with 14.2 mm radius was drilled through the rock along the X-axis at the center of the Y-Z plane, as shown in Figure 7. Uniaxial stress, which is applied along Z-axis, is perpendicular to the borehole axis. The stress is also raised in steps of 0.96 MPa up to 10.6 MPa. Strain measurements are made at four locations represented by A, B, C and D, as shown in Figure 7. We applied our work flow illustrated in Figure 1 and used a FEM software to numerically calculate the stress-induced anisotropy around the borehole subjected to uniaxial stress.

Figure 8 shows the convergence (equation 4) of the iterations at eleven loading stresses. We found that the convergence is very fast and the change of model stiffness is less than 1% after the first two iterations. We will show the results obtained after the fifth iteration. Figure 9 shows the simulated principal normal stresses σ_{yy} and σ_{zz} on the borehole model surface under 10.6 MPa stress loading in the Z direction. Let $\theta = 0^0$ define the direction of the applied stress. As seen in Figure 9c, the circumferential stress is highly compressive at $\theta = \pm 90^0$ while it is tensile at $\theta = 0^0$ and 180^0. The stress around the borehole now is strongly spatially dependent. As a result, each point over space, initially elastic isotropic in the unstressed state, now becomes anisotropic due to the varying local stress field.

In Figure 10, the strains measured at four different positions A, B, C and D are compared to the numerical simulations, similar to Figure 7. We find a good match between the measurements and numerical simulations. Strains measured at B and C, roughly 6 mm away from the borehole edge, are strongly affected by the stress alteration around the borehole. The strain $e_{||}$ at B in absolute value is much larger than those at A, C and D, and it reaches a minimum value at C. This is because stress is highly concentrated at B and released at C, as shown in Figure 9b. The strain $e_{||}$ at D is smaller than that at A. This is again due to the alteration of stress concentration around the borehole. The strain $e_{\perp}$ always seems to be underestimated in the numerical calculations, perhaps due to the neglect of crack opening, similar to Figure 6. Our numerical results, however, are a very reasonable match with the measurements. This suggests that the neglect of crack opening has a minor effect in our approach.

Winkler (1996) measured the compressional wave velocity versus azimuth around a borehole in Berea sandstone with applied uniaxial stress. In his experiment, a block of Berea sandstone (15×15×13 cm) with a 2.86 cm diameter borehole parallel to the short dimension was saturated in a water tank for conducting acoustic measurements. The P-wave velocity at each azimuth was measured along the borehole axis by using directional transducers. Some properties of the rock are shown in Table 2. Figure 11 shows the measured P-wave velocity versus azimuth with no stress loading (open circles) and with 10 MPa stress loading (solid circles). The P-wave velocity variation with azimuth is very small before applying the stress, and its average value is about 2.54 km/s at no stress state. In the experiment of Winkler (1996), the center frequency of the received acoustic signals is about 250 kHz, the corresponding wave length is 1.02 cm, which is equal to $0.36D$ (D: borehole diameter). We define $\tilde{\lambda} = 0.36D$ as the characteristic wavelength for measuring P-wave

velocity. The size of the rock sample and borehole in our experiment is different from that in the experiment of Winkler (1996), therefore we compare our results through scaling the model by the borehole diameter. We calculate the spatial distribution of the stiffness tensor of our Berea sandstone borehole model with 10 MPa uniaxial stress applied. The velocity of a P-wave propagating along the borehole axis is mainly governed by the elastic constant C_{1111}, which is shown in Figure 12. From Figure 12, we can see that, near the wellbore, the rock becomes stiffer around the regions at $\theta = \pm 90^0$, while it is relatively softer at $\theta = 0^0$ and 180^0. Assuming that the P-wave velocity along X-axis direction is mainly governed by C_{1111}, then the P-wave velocity along the borehole axis direction is given as

$$V_P = \sqrt{\frac{C_{1111}}{\rho}} \tag{9}$$

where ρ is density, which is assumed to be independent of the applied stress.

Anisotropy and inhomogeneity of the rock around a borehole can cause dispersion. For a wave with wavelength $\tilde{\lambda} = 0.36D$, the penetration depth of the waves propagating along the borehole wall could be up to $1 \sim 2$ $\tilde{\lambda}$. Here, we first calculate the P-wave velocity by using equation 9 and then average the velocity at each azimuth to obtain the velocity variation with azimuth. The velocity averaging method is shown in Figure 12. In Figure 12, the black circle represents a circular area centered at the wellbore at $\theta = 0^0$ with radius r, which represents the penetration depth of the waves, the velocity at $\theta = 0^0$ is taken as the average of the velocity inside the black circle. By moving this black circle from $\theta = 0^0$ to 360^0, a scan of the velocity versus azimuth can be obtained. By choosing different values of r, we can obtain the variation of P-wave velocity around the borehole with different penetration depth. We choose $r = \tilde{\lambda}$, $1.5\tilde{\lambda}$ and $2\tilde{\lambda}$ to do the averaging separately

over different areas, which are shown as the red, blue and magenta circles in Figure 12, respectively. The predicted average velocities normalized by the P-wave velocity with no applied stress are plotted in Figure 13 together with the data measured by Winkler (1996). Winkler (1996) used a $\cos(2\theta)$ function, shown as the black curve in Figure 13, to fit the data based on the $\cos(2\theta)$ dependence of σ_θ and σ_r on θ in equations 5 and 6. Red, blue and magenta curves are the velocities obtained from our model by using different averaging radii r. The azimuthal velocity variation decreases away from the wellbore, so a larger averaging radius r gives smaller velocity variation. $r = 1.5\tilde{\lambda}$ could be a reasonable averaging radius. The mismatch between the blue curve and the black best fit curve is larger at θ=0^0 and 180^0, this may be caused by the neglect of crack opening in our calculation.

CONCLUSIONS

An isotropic rock becomes anistropic when subjected to an anisotropic applied stress, which causes crack closure or opening and induces elastic anisotropy. The presence of a borehole alters the local stress field and leads to inhomogeneous anisotropy distribution around it. In this paper, we present a numerical approach to predict the stress-induced anisotropy around a borehole given a stress state by applying the method of Mavko et al. (1995). Our method uses hydrostatic data (*i.e.* V_P and V_S), which are easy to obtain, to calculate the distribution of this stress-induced anisotropy around a borehole. The accuracy of the our method is validated through laboratory experiments on a Berea sandstone sample. Our approach can predict the stress-strain relation around a borehole in Berea sandstone under uniaxial stress reasonably well. Our method can be applied to calculate the spatially varying anisotropic elastic constants which are required for the forward modeling of wave propagation in a borehole under a given stress state. Also, this could potentially provide a

physical basis for using acoustic cross-dipole logging to estimate the *in situ* stress state.

ACKNOWLEDGMENTS

We thank Dan Burns for helpful discussion. Tianrun Chen was supported by an ERL Founding Member postdoctoral fellowship.

REFERENCES

Birch, F., 1960, The velocity of compressional waves in rocks to 10 kbar, 2: J. geophys. Res, **65**, 1083–1102.

Brace, W., and D. Kohlstedt, 1980, Limits on lithospheric stress imposed by laboratory experiments: Journal of Geophysical Research, **85**, 6248–6252.

Brown, S., and A. Cheng, 2007, Velocity anisotropy and heterogeneity around a borehole: SEG Technical Program Expanded Abstracts, **26**, 318–322.

Jaeger, J., N. Cook, and R. Zimmerman, 2007, Fundamentals of rock mechanics: Wiley-Blackwell.

Mao, N., 1987, Shear wave transducer for stress measurements in boreholes. (US Patent 4,641,520).

Mavko, G., T. Mukerji, and N. Godfrey, 1995, Predicting stress-induced velocity anisotropy in rocks: Geophysics, **60**, 1081.

Oda, M., 1986, An equivalent continuum model for coupled stress and fluid flow analysis in jointed rock masses: Water resources research, **22**, 1845–1856.

Oda, M., T. Yamabe, and K. Kamemura, 1986, A crack tensor and its relation to wave velocity anisotropy in jointed rock masses: Int. J. Rock. Mech. Min. Sci, **23**, 387–397.

Sayers, C., J. Van Munster, and M. King, 1990, Stress-induced ultrasonic anisotrophy in berea sandstone: International Journal of Rock Mechanics and Mining Sciences & Geomechanics Abstracts, Elsevier, 429–436.

Sinha, B., and S. Kostek, 1995, Identification of stress induced anisotropy in formations. (US Patent 5,398,215).

———, 1996, Stress-induced azimuthal anisotropy in borehole flexural waves: Geophysics, **61**, 1899.

Tang, X., and C. Cheng, 2004, Quantitative borehole acoustic methods: Pergamon.

Tang, X., N. Cheng, and A. Cheng, 1999, Identifying and estimating formation stress from borehole monopole and cross-dipole acoustic measurement: SPWLA 40th.

Wang, Z., 2002, Seismic anisotropy in sedimentary rocks, part 2: Laboratory data: Geophysics, **67**, 1423.

Winkler, K., 1996, Azimuthal velocity variations caused by borehole stress concentrations: Journal of geophysical research, **101**, 8615–8621.

Winkler, K., B. Sinha, and T. Plona, 1998, Effects of borehole stress concentrations on dipole anisotropy measurements: Geophysics, **63**, 11.

Zoback, M., D. Moos, L. Mastin, and R. Anderson, 1985, Well bore breakouts and in situ stress: Journal of Geophysical Research, **90**, 5523–5530.

Table 1: Summary of parameters of the Berea sandstone sample in unstressed state.

Dimensions (mm)	V_p	V_s	Density	Poission's ratio	Porosity	Permeability
$101.4 \times 100.6 \times 102.3$	2.83 km/s	1.75 km/s	2.198 g/cm^3	0.19	17.7%	284 mD

Table 2: Properties of the rock sample used by Winkler (1996)

V_p (no stress)	Porosity	Permeability
2.54 km/s	22 %	510 mD

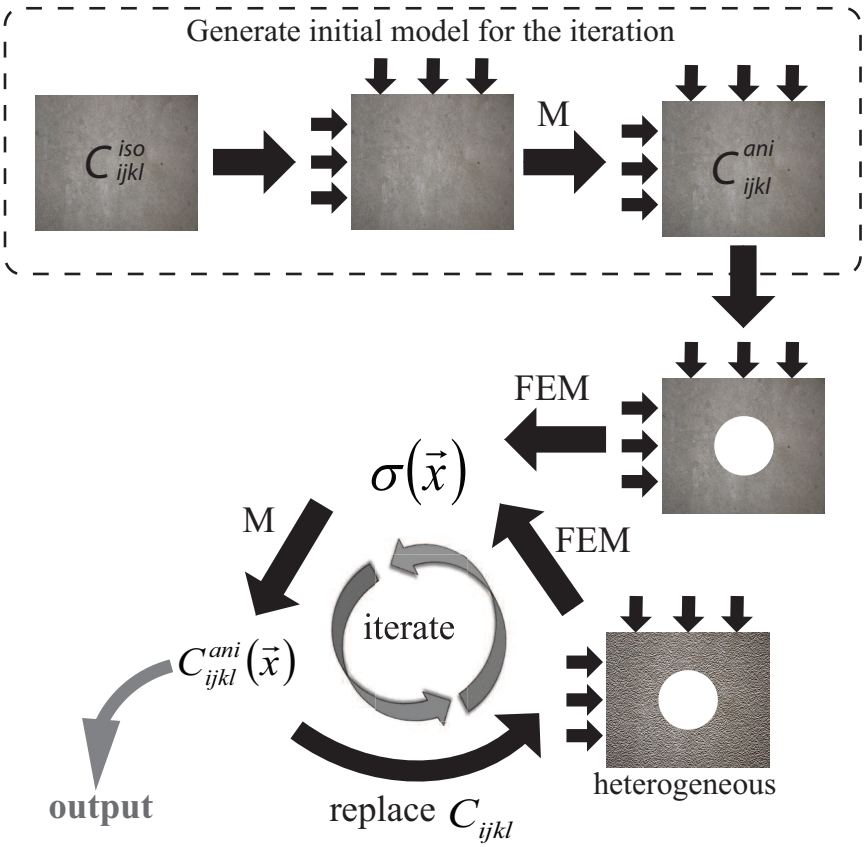

Figure 1: Workflow for computation of stress-induced anisotropy around a borehole. 'FEM' and 'M' represent finite-element method and the method of Mavko et al. (1995), respectively. See text for explanation.

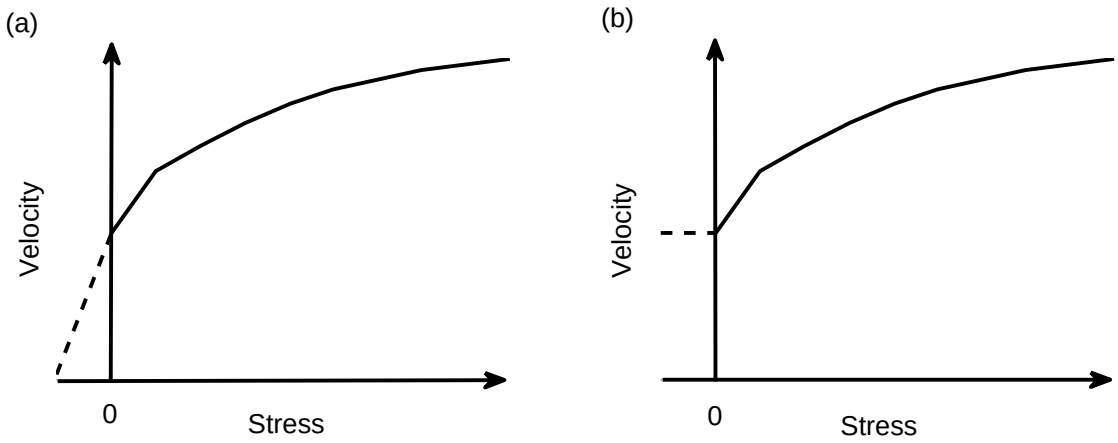

Figure 2: Schematic showing two ways to predict the velocity under tensile stress. Solid curves represent the data measured in compression (stress>0) experiment, dashed lines indicate the extrapolation of data to tensile stress (stress<0) region. (a) velocity decreases with the decreasing of stress and (b) velocity is constant when stress<0.

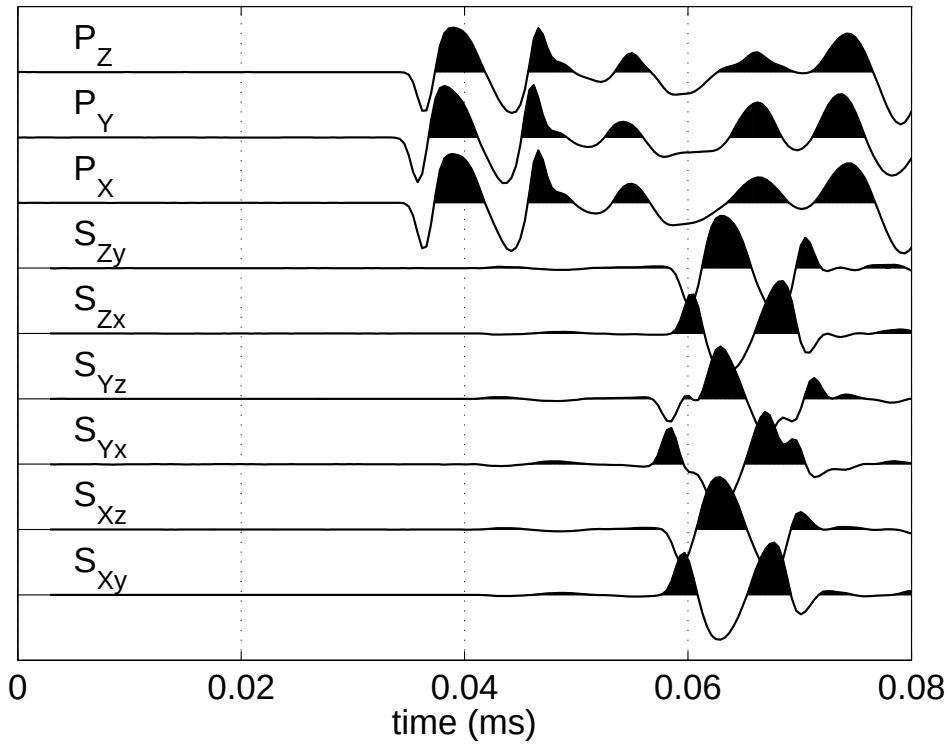

Figure 3: Traces recorded for measuring the compressional and shear velocities of the Berea sandstone sample. Acoustic measurements were conducted in three orthogonal directions. P_i (i=X,Y,Z) indicates the measurement of P-wave along i direction, and S_{ij} (i,j=X,Y,Z) indicates the measurement of S-wave along i direction with polarization in j direction.

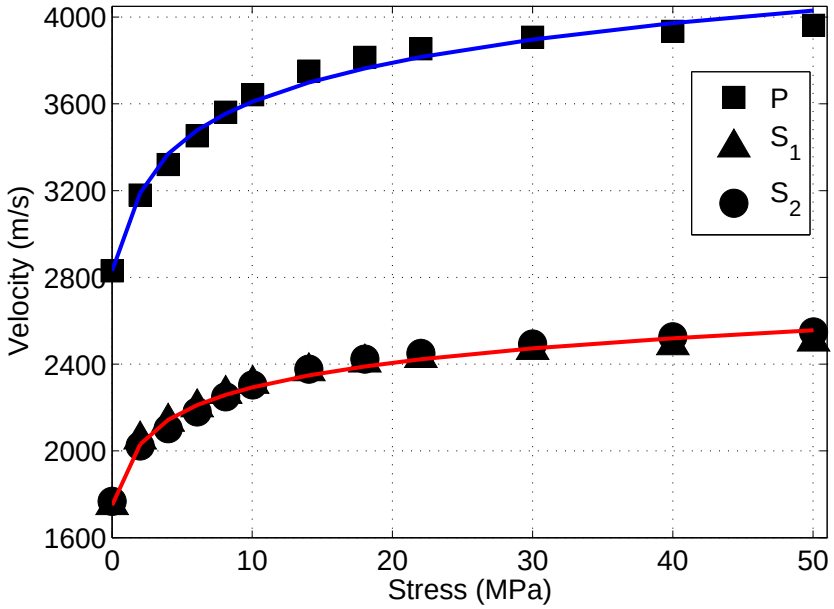

Figure 4: Measurements of P-wave (squres) and S-wave (triangles and circles) velocities of the Berea sandstone core sample under hydrostatic compression. All measurements were conducted along the core axis direction. Shear wave velocities S_1 and S_2 were measured along the same propagation direction but with orthogonal polarization directions. Blue and red curves are the fitting curves (equation 8) to the P-wave and S-wave velocities (average of S_1 and S_2) respectively. The root-mean-square misfits are, respectively, 38 m/s and 18 m/s for the fits to P and S-wave velocities.

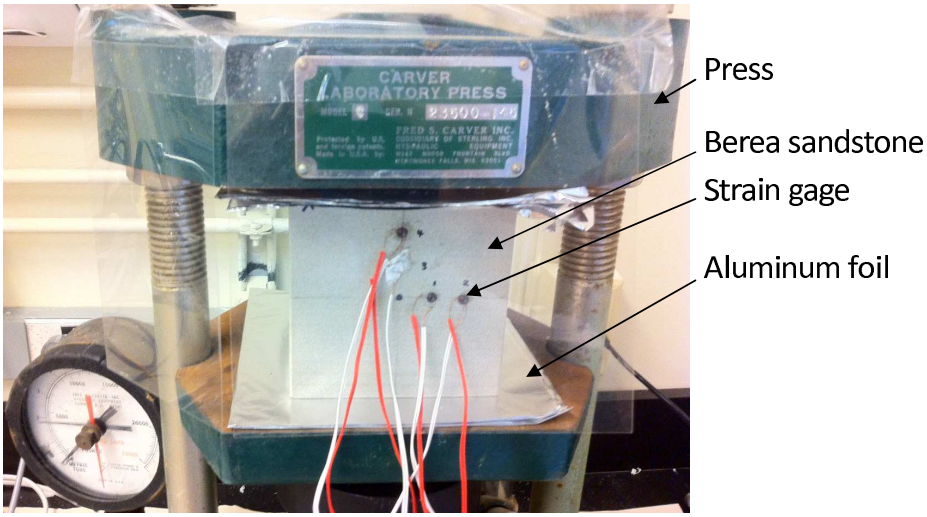

Figure 5: Photo of experiment setup. The Berea sandstone sample is a 10 cm cube. The size of the strain gage is about 2 mm. The aluminum foil between the press and the rock is used to make the loading pressure distribution more uniform on the rock surface.

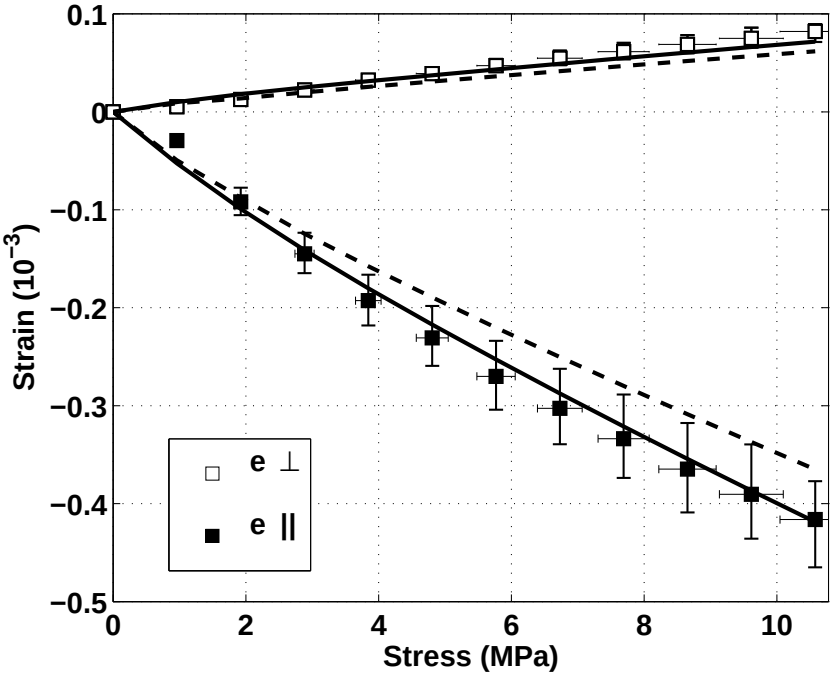

Figure 6: Average normal strains of the intact rock sample under uniaxial loading. Solid and open squares are the measured strain in the directions parallel and normal to the loading stress respectively. Error bars represent estimates of errors from uncertainty in the measurement of loading stress ($\sim 5\%$) and the error of the gage factor ($\sim 1\%$). Solid curves and dashed curves are the predicted values obtained from the anisotropic model and isotropic model, respectively.

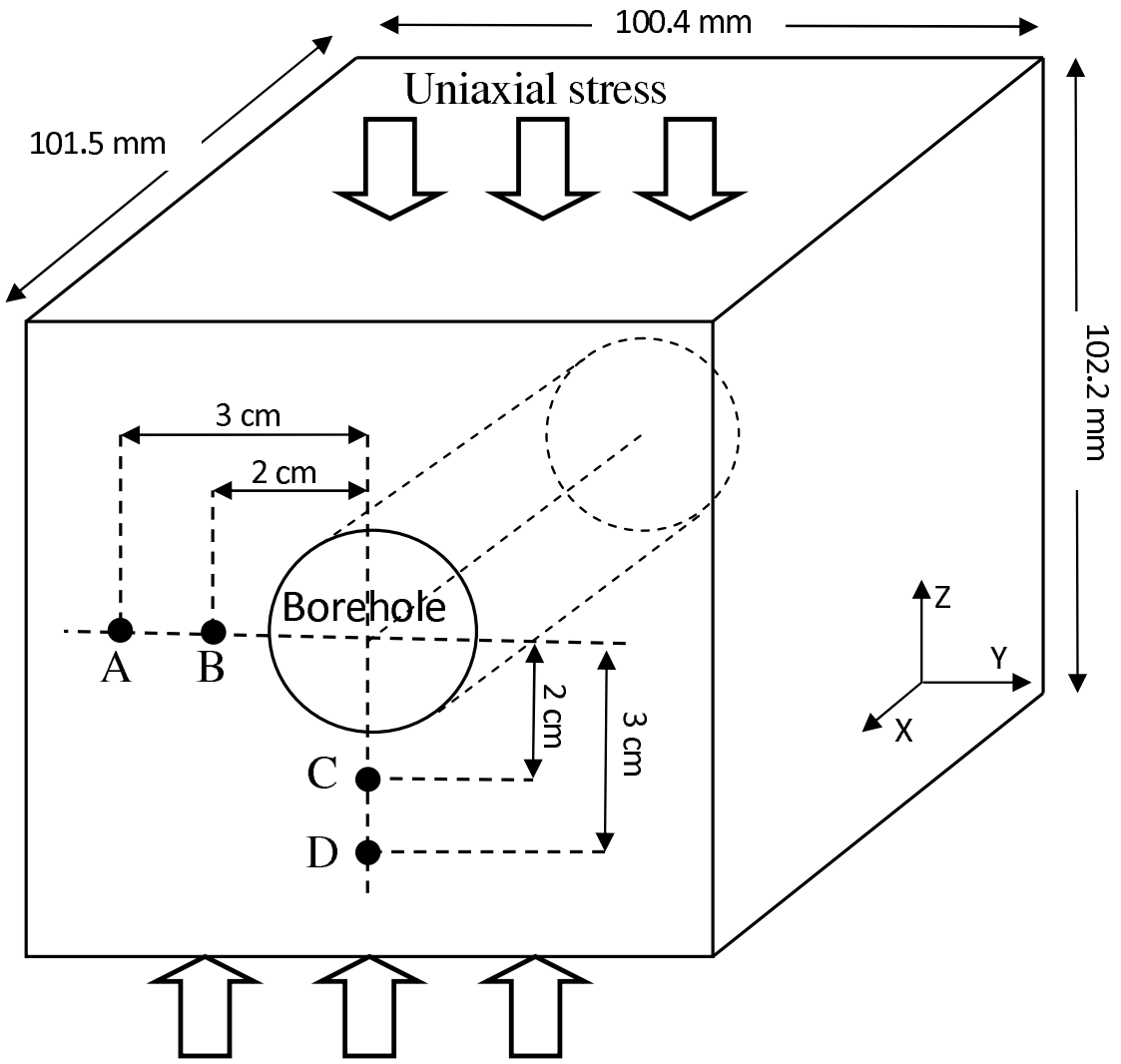

Figure 7: Schematic showing uniaxial stress loading on a rock sample with a borehole. The borehole axis, which is along X-axis, is normal to the loading stress direction. Strain measurements are conducted at locations A, B, C and D. B and C are 2 cm away from the borehole center, A and D are 3 cm away from the borehole center. Borehole radius is 14.2 mm.

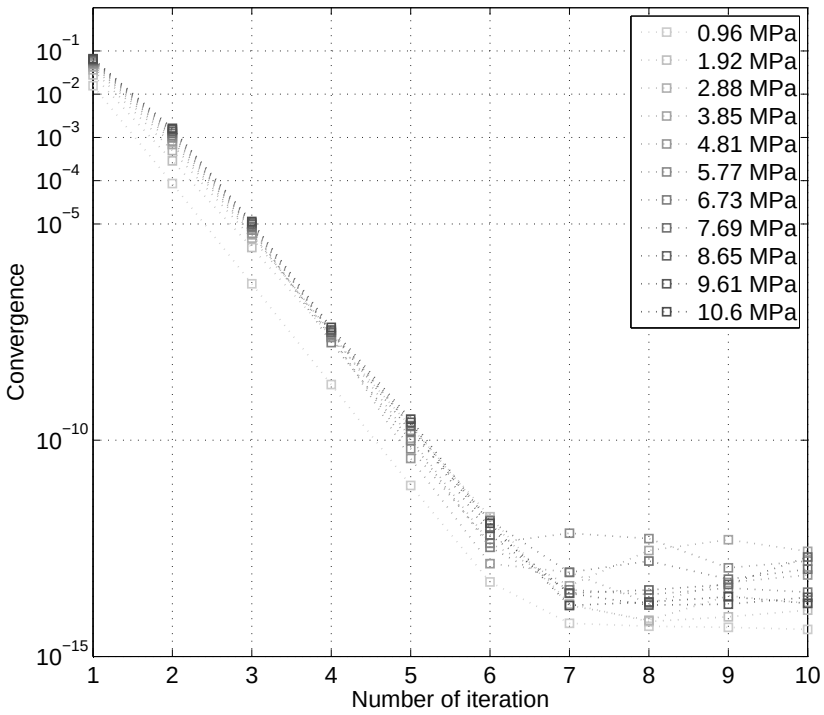

Figure 8: Convergence of the iteration scheme under different loading stress strength. Convergence, which is defined by equation 4, describes the percentage change of the model stiffness after each iteration.

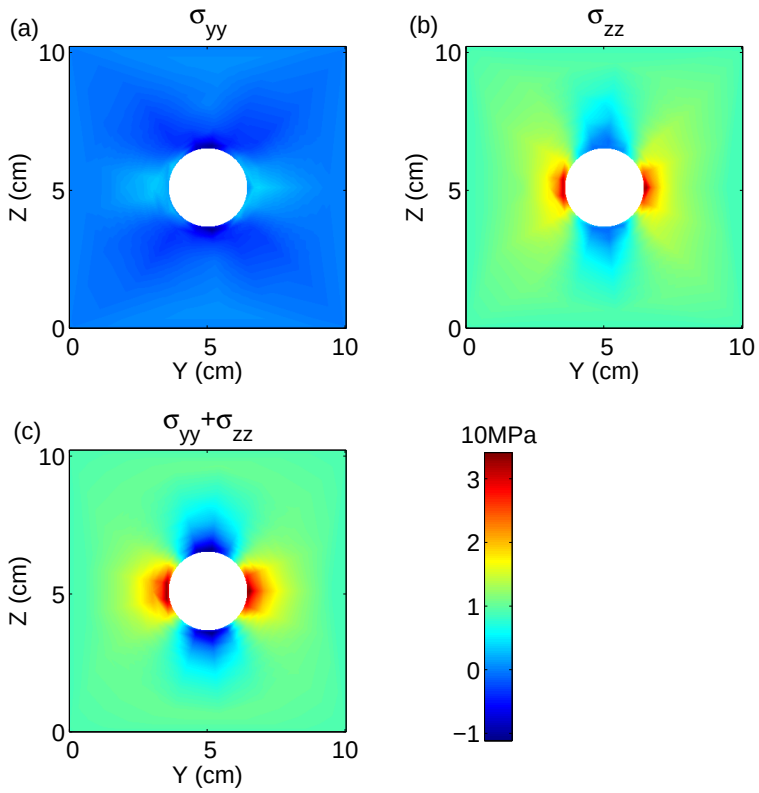

Figure 9: (a) and (b) show the distribution of σ_{yy} and σ_{zz}, which are the normal stresses in Y and Z directions, under 10.6 MPa uniaxial stress loading. (c) is the sum of σ_{yy} and σ_{zz}.

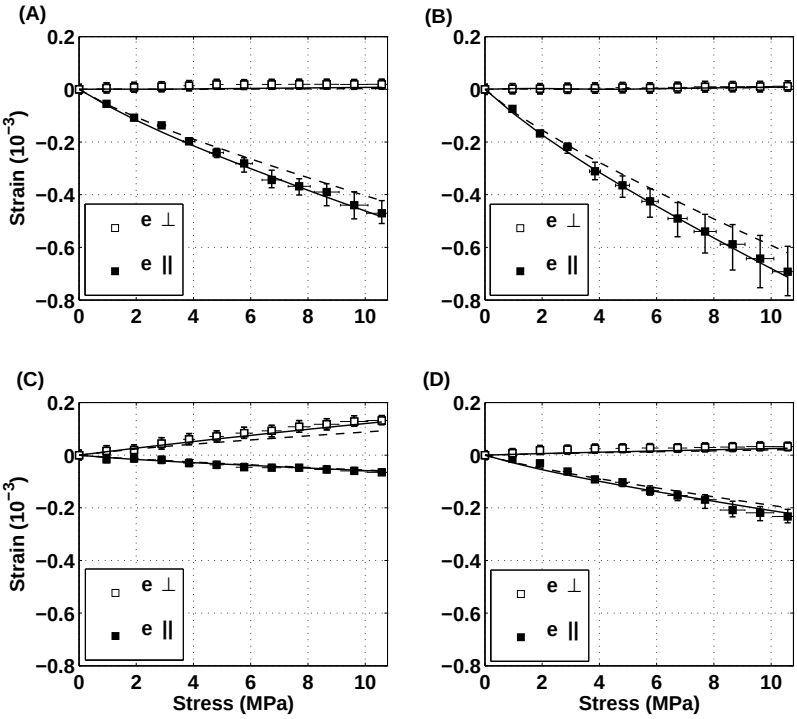

Figure 10: Comparison of laboratory measured strains and numerical results at locations A, B, C and D, which are shown in Figure 7. Solid and open squares are the measured strain in the directions parallel and normal to the loading stress respectively. Error bars represent estimates of errors from uncertainty in the measurement of loading stress ($\sim 5\%$) and the error of the gage factor ($\sim 1\%$). Solid curves and dashed curves are the predicted values obtained from the anisotropic model and isotropic model, respectively.

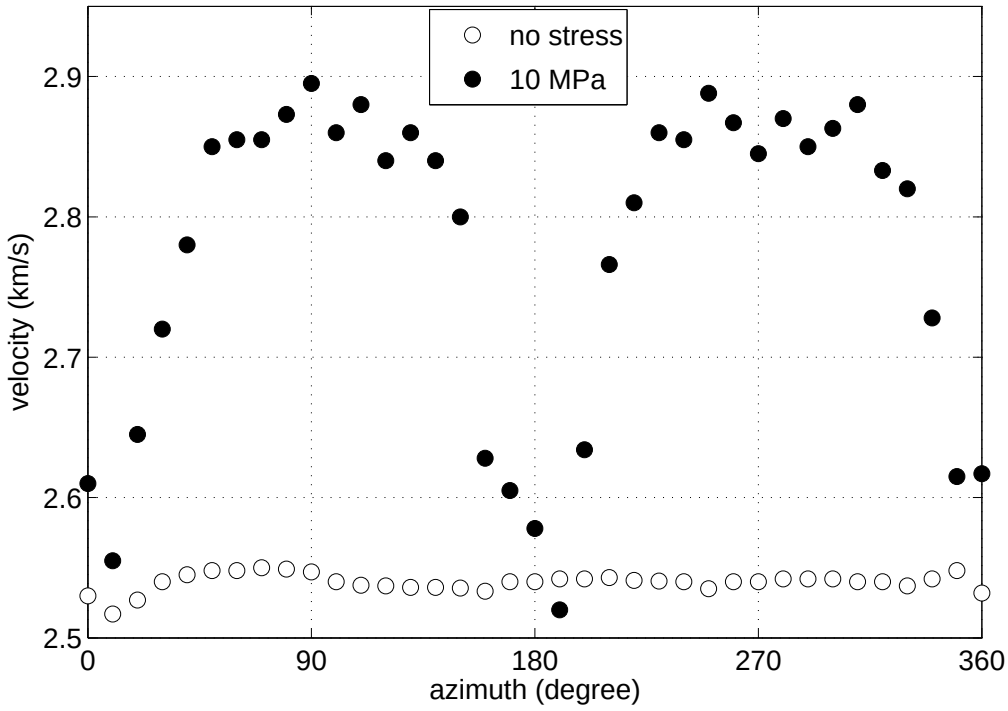

Figure 11: Compressional wave velocity versus azimuth data measured on Berea sandstone with no stress loading (open circles) and with 10 MPa uniaxial stress (solid circles). 0 and 180 degree are along the loading stress direction, 90 and 270 degree are normal to the stress direction. Data are taken from the paper of Winkler (1996).

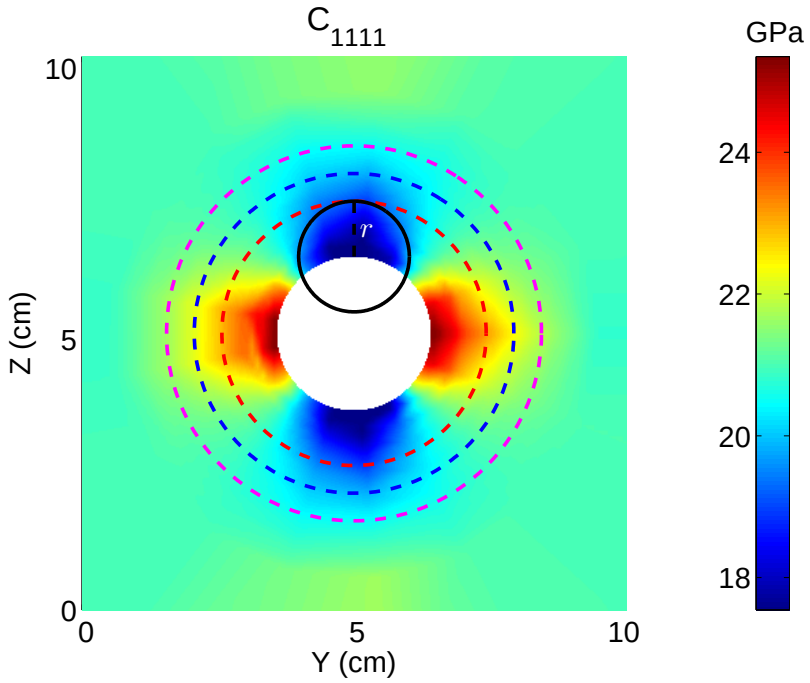

Figure 12: Plot of the elastic constant C_{1111} in the Y-Z profile under 10 MPa uniaxial stress loading in Z direction. Circles show how the P-wave velocity is calculated through averaging over a region. Black circle represents a circular region centering at the wellbore at θ=0^0 with radius r, the average of P-wave velocity inside the circle, not including the white area, is taken as the P-wave velocity at $\theta = 0^0$, and the P-wave velocities versus azimuth are obtained by doing this averaging over θ from 0^0 to 360^0. Red, blue and magenta dashed circles indicate the averaging regions for r=$\tilde{\lambda}$, $1.5\tilde{\lambda}$ and $2\tilde{\lambda}$, respectively.

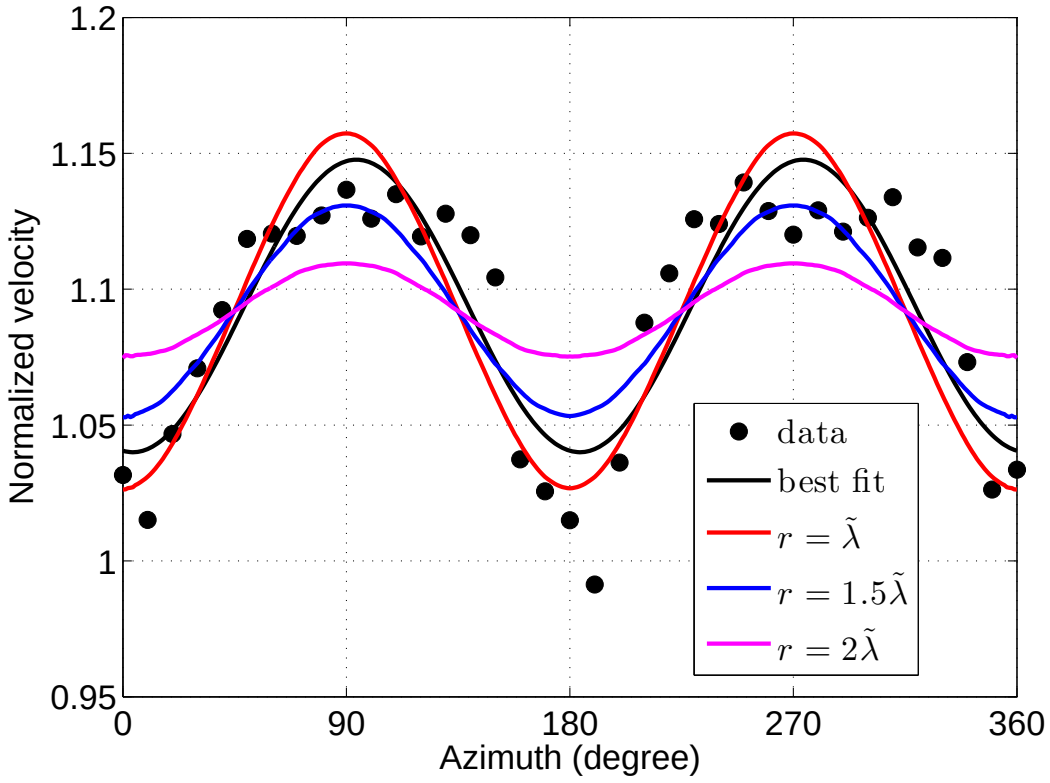

Figure 13: Solid circles are the normalized compressional wave velocity (normalized by the velocity measured at 0 stress state) measured by Winkler (1996) under 10 MPa uniaxial stress. Black curve is the best fit to the data by using a cosine function. Red, blue and magenta curves show the normalized velocities of the Berea sandstone used in our experiment by using r=$\tilde{\lambda}$, $1.5\tilde{\lambda}$ and $2\tilde{\lambda}$, respectively, in the averaging.